



# Existence regime of symmetric and asymmetric Taylor vortices in wide-gap spherical Couette flow

Suhail Abbas<sup>1,2</sup> · Li Yuan<sup>1,2</sup> · Abdullah Shah<sup>3</sup>

Received: 30 November 2017 / Accepted: 10 February 2018  
© The Brazilian Society of Mechanical Sciences and Engineering 2018

## Abstract

We study the existence regime of symmetric and asymmetric Taylor vortices in wide-gap spherical Couette flow by time marching the three-dimensional incompressible Navier–Stokes equations numerically. Three wide-gap clearance ratios,  $\beta = (R_2 - R_1)/R_1 = 0.33, 0.38$  and  $0.42$  are investigated for a range of Reynolds numbers respectively. Using the 1-vortex flow for clearance ratio  $\beta = 0.18$  at Reynolds number  $Re = 700$  as the initial conditions and suddenly increasing  $\beta$  to the target value, we can compute Taylor vortices for the three wide gaps. For  $\beta = 0.33$ , Taylor vortices exist in the range  $450 \leq Re \leq 2050$ . With increasing  $Re$  the steady symmetric 1-vortex flow becomes steady asymmetric at  $Re = 1850$ , and then become periodic at  $Re = 2000$ . When  $Re > 2050$  the flow returns back to the steady basic flow state with no Taylor vortices. For  $\beta = 0.38$ , Taylor vortices can exist in the range  $500 \leq Re \leq 1400$ . With increasing  $Re$ , the steady symmetric 1-vortex flow become steady asymmetric at  $Re = 1200$ , and then the flow evolves into the steady basic flow for  $Re > 1400$ . For  $\beta = 0.42$ , Taylor vortices can exist in the range  $650 \leq Re \leq 1300$ . With increasing  $Re$ , steady asymmetric Taylor vortices occur at  $Re = 1150$ , and then the flow evolves into the steady basic flow for  $Re > 1300$ . The present numerical results are in good agreement with available numerical and experimental results. Furthermore, the existence regime of Taylor vortices in the  $(\beta, Re)$  plane for  $\beta \geq 0.33$  and the three-dimensional transition process from periodic asymmetric vortex flow to steady basic flow with increasing  $Re$  are presented for the first time.

**Keywords** Spherical Couette flow · Wide gap · Symmetric Taylor vortices · Asymmetric Taylor vortices

## List of symbols

$J$	Determinant of coordinate transformation Jacobian	$Re_c$	Critical Reynolds number
$p$	Pressure	$t$	Physical time
$R_1$	Radius of inner sphere	$U, V, W$	Contra-variant velocity components
$R_2$	Radius of outer sphere	$\alpha$	Artificial compressibility factor
$r, \theta, \phi$	Spherical coordinates	$\beta = (R_2 - R_1)/R_1$	Clearance ratio
$Re = \Omega R_1^2/\nu$	Reynolds number	$\beta_w$	Lower bound value for wide-gap clearance ratio
		$\nu$	Kinematic viscosity
		$\tau$	Pseudo time
		$\omega_\phi$	Azimuthal vorticity component
		$\Omega$	Angular velocity

Technical Editor: Jader Barbosa Jr.

✉ Li Yuan  
lyuan@lsec.cc.ac.cn

- <sup>1</sup> LSEC and Institute of Computational Mathematics and Scientific/Engineering Computing, Academy of Mathematics and Systems Science, Chinese Academy of Sciences, Beijing 100190, People's Republic of China
- <sup>2</sup> School of Mathematical Sciences, University of Chinese Academy of Sciences, Beijing 100190, People's Republic of China
- <sup>3</sup> Department of Mathematics, COMSATS Institute of Information Technology, Islamabad, Pakistan

## 1 Introduction

Spherical Couette flow is induced between the annulus of two concentric spheres by rotating one sphere or both. When we look at the geometry of the spherical Couette flow, it is similar to a rotating disk in a stationary casing in the polar region while it is similar to a cylindrical circular

Couette flow in the equatorial region. The spherical Couette flow is a typical problem in the study of hydrodynamic instabilities, and is relevant to a wide range of applications in planetary atmospheres, geophysics, astrophysics, and engineering problems [1–3].

A lot of work has been done on the spherical Couette flow in the past, but most of them were restricted to narrow- and medium-gap clearance ratios [4–22]. A limited number of studies were conducted for wide-gap clearance ratios [3, 9, 23–33]. The flow instabilities occurring strongly depend on the Reynolds number ( $Re$ ) and the gap clearance ratio ( $\beta$ ). Nakabayashi et al. [34] summarized the classification of spherical gaps in detail. They took  $\beta_W \approx 0.3$  as the boundary between medium and wide gaps. This value of  $\beta_W$  is adopted in this paper. Many experimental studies showed that the Taylor instability occurs as the first instability for narrow and medium gaps ( $\beta < \beta_W$ ), and the cross-flow instability occurs as the first instability for wide gaps ( $\beta > \beta_W$ ).

The occurrence of the Taylor instability for wide-gap clearance ratios was studied by a few researchers. For example, Schrauf [9] first obtained one pair of Taylor vortices for wide gaps ( $\beta = 0.45 - 0.48$ ) using an axisymmetric continuation solver. Hollerbach [30] used a spectral code to compute symmetric and asymmetric 1-vortex flows for  $\beta = 0.336$  in the range  $415 \leq Re \leq 2040$  using the 1-vortex flow easily obtained for  $\beta = 0.154$  as the initial conditions and increasing  $\beta$  gradually to  $\beta = 0.336$ . They noticed that the asymmetric vortices become time dependent for  $1940 \leq Re \leq 2035$ , and for  $Re > 2040$  the time dependent asymmetric vortex flow collapses back to the basic flow. Loukopoulos and Karahalios [32] numerically investigated the symmetric and asymmetric 1-vortex flows for  $\beta = 0.38, 0.42$  and  $0.48$  by counter-rotating the outer sphere temporarily and then reducing its angular velocity to zero. They have provided the range of Reynolds number in which these symmetric and asymmetric 1-vortex flows exist. However, these numerical studies used the axisymmetric assumption.

The first experimental Taylor vortices for  $\beta = 0.33$  were obtained by Liu et al. [31]. They used special initial conditions, i.e., rotating the outer sphere temporarily. They found that stable 1-vortex flows coexist in the range  $Re \in [470, 2100]$  with the basic flow state. Their work motivated the numerical work of Hollerbach [30]. Junk and Egbers [29] also got one pair of symmetric and asymmetric Taylor vortices experimentally by counter-rotating the outer sphere for a short period of time. They found that the 1-vortex flow remains stable in the range  $Re \in [470, 1850]$ , and with further increase of the Reynolds number the flow returns back to the basic flow state having no Taylor vortices at all.

Despite the fact that some numerical and experimental studies have verified the existence of symmetric and asymmetric Taylor vortices in wide gaps ( $\beta > 0.3$ ), yet three-dimensional numerical simulations of Taylor vortices in wide gaps are few even if the laminar–turbulent transition for  $\beta = 1$  had been simulated by Zhilenko [35]. The aim of this study is to investigate the existence regime in the  $(\beta, Re)$  plane for Taylor vortices in wide gaps and the transition detail from asymmetric vortex to basic flows with increasing  $Re$  via numerical solution of the three-dimensional incompressible Navier–Stokes equations. We use the artificial compressibility method incorporated with the weighted essentially non-oscillatory (WENO) finite difference scheme [36] and a line GS method [37]. The numerical results reveal that with increasing  $\beta$ , the upper bound of  $Re$  for the existence of Taylor vortices decreases while the lower bound increases so that the two bounds will merge into each other at a large value of  $\beta$  ( $\approx 0.48$ ), after which only the cross-flow instability [23] occurs as the first instability. Further, the three-dimensional transition detail from asymmetric vortex flows to basic flows with increasing  $Re$  is given for the first time. Our numerical results also provide the detail of the vortex fluctuations in the equatorial region as first found by Hollerbach [30].

## 2 Geometrical configuration, governing equations and numerical method

### 2.1 Geometrical configuration

We consider the spherical Couette flow as shown in Fig. 1, where the inner sphere is rotating and the outer one is stationary. The flow behaviour can be characterized by two

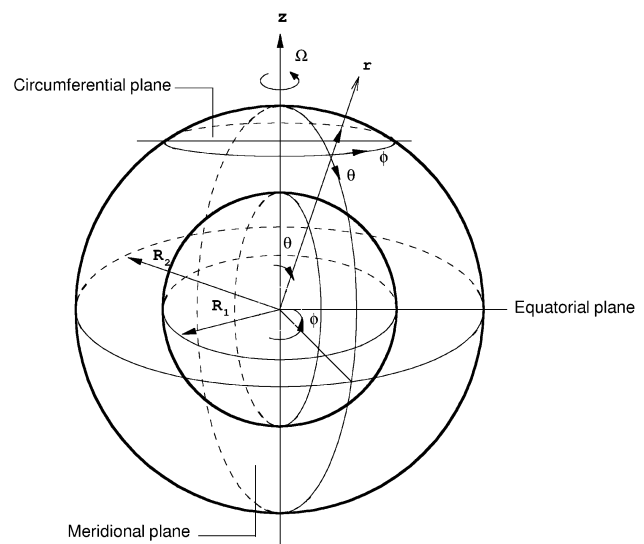


Fig. 1 The geometry of spherical Couette flow system

control parameters, the gap clearance ratio  $\beta \equiv (R_2 - R_1)/R_1$  and the Reynolds number  $Re \equiv \Omega R_1^2/\nu$ , where  $R_1, R_2$  are the radii of the inner and outer spheres, respectively,  $\Omega$  is the angular velocity of the inner sphere,  $\nu$  is the kinematic viscosity of the fluid.

### 2.2 Governing equations and numerical method

The governing equations are the three-dimensional incompressible Navier–Stokes equations, which are written in strong conservative form in the generalized orthogonal curvilinear coordinates  $\xi, \eta$  and  $\zeta$  using the artificial compressibility method [38],

$$\partial_\tau \hat{\mathbf{Q}} + \mathbf{I}_m \partial_t \hat{\mathbf{Q}} + \partial_\xi (\hat{\mathbf{E}} - \hat{\mathbf{E}}_v) + \partial_\eta (\hat{\mathbf{F}} - \hat{\mathbf{F}}_v) + \partial_\zeta (\hat{\mathbf{G}} - \hat{\mathbf{G}}_v) = \mathbf{0}, \tag{1}$$

where

$$\begin{aligned} \hat{\mathbf{Q}} &= \frac{\mathbf{Q}}{J} = \frac{1}{J} \begin{bmatrix} p \\ u \\ v \\ w \end{bmatrix}, \hat{\mathbf{E}} = \frac{1}{J} \begin{bmatrix} \alpha U \\ Uu + \xi_x p \\ Uv + \xi_y p \\ Uw + \xi_z p \end{bmatrix}, \\ \hat{\mathbf{F}} &= \frac{1}{J} \begin{bmatrix} \alpha V \\ Vu + \eta_x p \\ Vv + \eta_y p \\ Vw + \eta_z p \end{bmatrix}, \hat{\mathbf{G}} = \frac{1}{J} \begin{bmatrix} \alpha W \\ Wu + \zeta_x p \\ Wv + \zeta_y p \\ Ww + \zeta_z p \end{bmatrix}, \\ \mathbf{I}_m &= \text{diag}(0, 1, 1, 1), \hat{\mathbf{E}}_v = \frac{1}{ReJ} (\nabla_\xi \cdot \nabla_\xi) \mathbf{I}_m \frac{\partial \mathbf{Q}}{\partial \xi}, \\ \hat{\mathbf{F}}_v &= \frac{1}{ReJ} (\nabla_\eta \cdot \nabla_\eta) \mathbf{I}_m \frac{\partial \mathbf{Q}}{\partial \eta}, \hat{\mathbf{G}}_v = \frac{1}{ReJ} (\nabla_\zeta \cdot \nabla_\zeta) \mathbf{I}_m \frac{\partial \mathbf{Q}}{\partial \zeta}, \\ U &= \xi_x u + \xi_y v + \xi_z w, V = \eta_x u + \eta_y v + \eta_z w, \\ W &= \zeta_x u + \zeta_y v + \zeta_z w. \end{aligned} \tag{2}$$

$\mathbf{Q} = (p, u, v, w)^T$  is the solution vector,  $u, v, w$  are the Cartesian velocity components,  $t$  is the physical time,  $\tau$  is the pseudo-time,  $\alpha$  is the artificial compressibility factor,  $U, V$  and  $W$  are the contra-variant velocity components in the  $\xi, \eta$  and  $\zeta$  directions, respectively.  $J$  is the Jacobian determinant of coordinate transformation. Further detail of the formulations can be found in Refs. [37, 39–41].

We use a finite difference weighted non-oscillatory (WENO) scheme [36, 42] for the convective terms, and a second-order central finite difference scheme for the viscous terms. An implicit backward difference scheme is used for the pseudo-time derivative and a second order, three-point backward difference scheme is used for the physical time derivative. The discretized equations are solved using the line Gauss–Seidel method as detailed in [37, 40]. The GS sweep process is parallelized with a pipeline method using OpenMP.

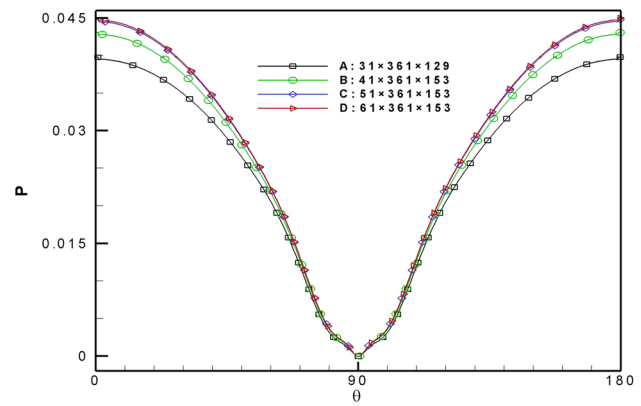


Fig. 2 Grid convergence of the pressure distribution on the inner wall with four different grid points for the steady symmetric 1-vortex flow at  $\beta = 0.42, Re = 650$

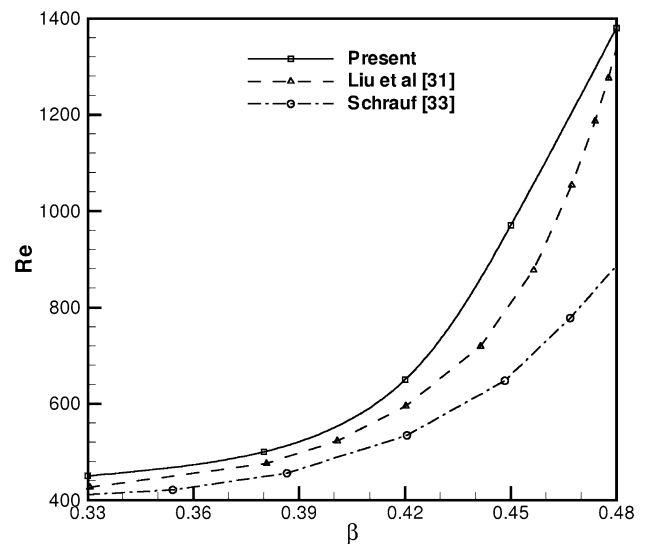
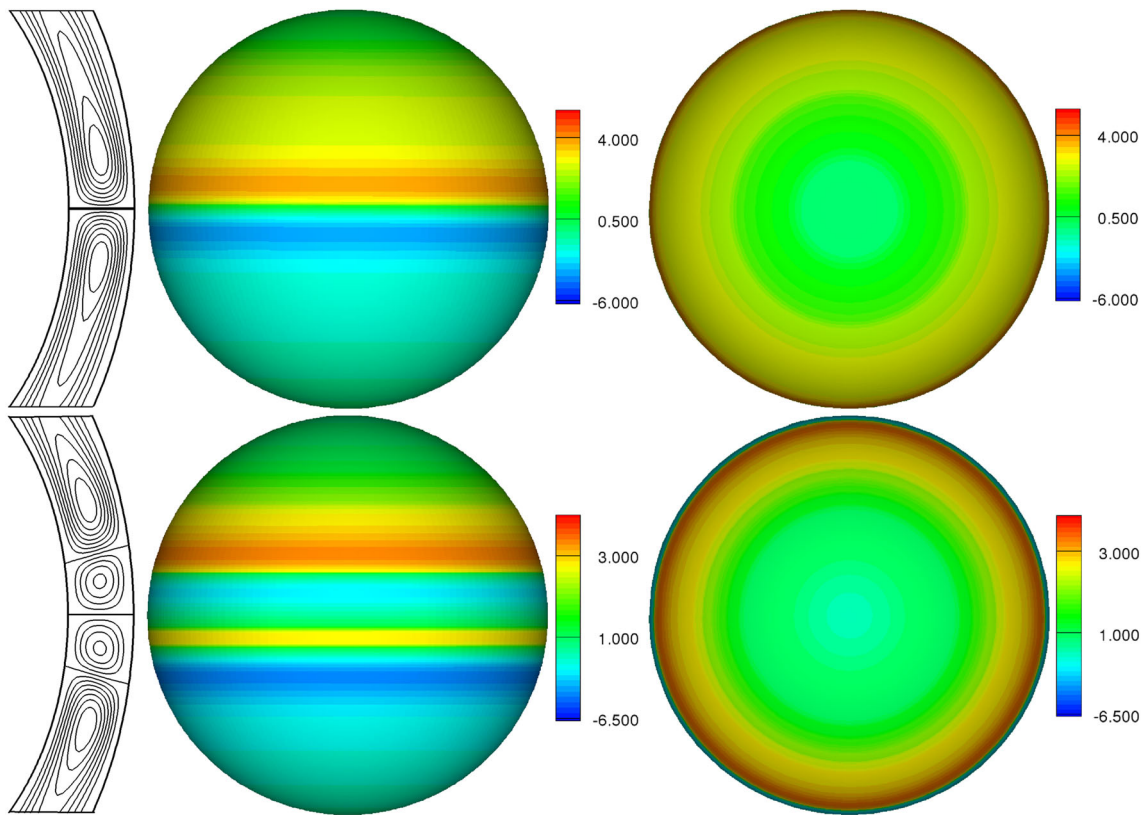


Fig. 3 Comparison of the lower boundary of the existence regime of Taylor vortices in the  $(\beta, Re)$  plane

No-slip boundary conditions are applied to the velocities on the outer and inner spheres. Pressure on the wall is obtained from the radial component of the momentum equations in the spherical coordinate system. A reference pressure is taken at a fixed point in the interior of the computational domain. The boundary condition on the polar axis is treated by setting values on the axis equal to averaging the neighboring points next to the axis.

### 2.3 Grid convergence

The spherical annulus is divided into grid points in the radial ( $r$ ), meridional ( $\theta$ ) and azimuthal ( $\phi$ ) directions, respectively. The grids points are clustered near the two walls along the radial direction where there are boundary layers. We have performed a grid convergence test to find a



**Fig. 4** Streamlines of symmetric 0-vortex and 1-vortex flows in the meridional plane ( $\phi = \pi$ ) in the equatorial region  $\frac{3\pi}{8} \leq \theta \leq \frac{5\pi}{8}$  at  $Re_{cl} = 450$  for  $\beta = 0.33$  on the left column, the middle column is

side-view of color contours of the azimuthal vorticity component ( $\omega_\phi$ ) at  $r = 1 + 0.5\beta$ , and the right column is the north pole view of it

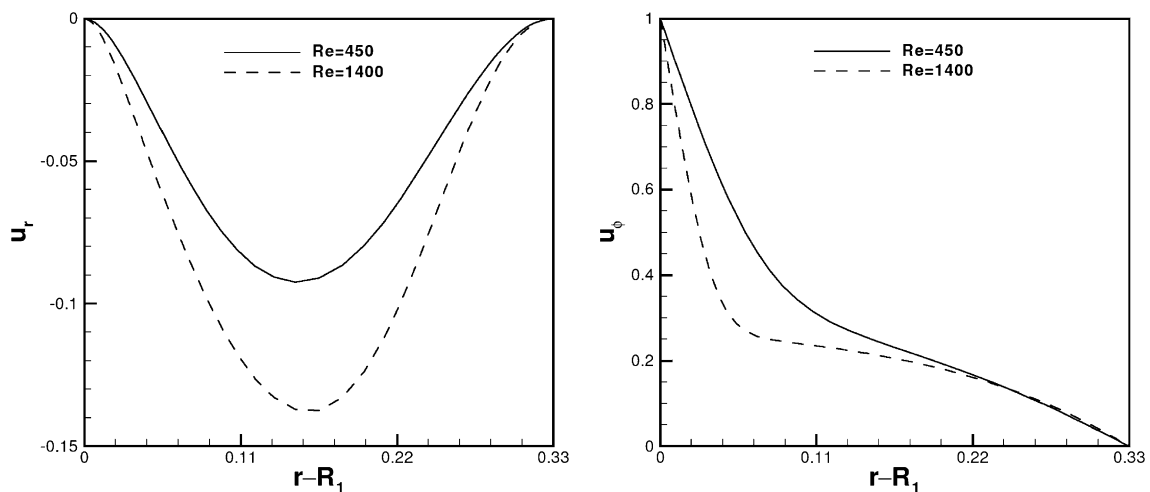


**Fig. 5** Distributions of the  $u_r$  velocity (left) and the  $u_\phi$  velocity (right) across the spherical gap for  $Re = 450$  and  $1400$  respectively,  $\beta = 0.33$

grid-independent solution. We tested four different grids, i.e.,  $31(r) \times 361(\theta) \times 129(\phi)$ ,  $41(r) \times 361(\theta) \times 153(\phi)$ ,  $51(r) \times 361(\theta) \times 153(\phi)$  and  $61(r) \times 361(\theta) \times 153(\phi)$  in the steady 1-vortex flow for  $\beta = 0.42$  at  $Re = 650$ . Figure 2 shows the inner wall pressure distribution along the meridional direction on four different grids. Clearly the

difference between solutions on grids C and D is negligible, and therefore, any grid resolution greater than or equal to  $51(r) \times 361(\theta) \times 153(\phi)$  can be used for simulation.

In this work, we use a grid number of  $51(r) \times 361(\theta) \times 153(\phi)$ . The non-dimensional physical time step  $\Delta t = 0.05$  and the artificial compressibility factor

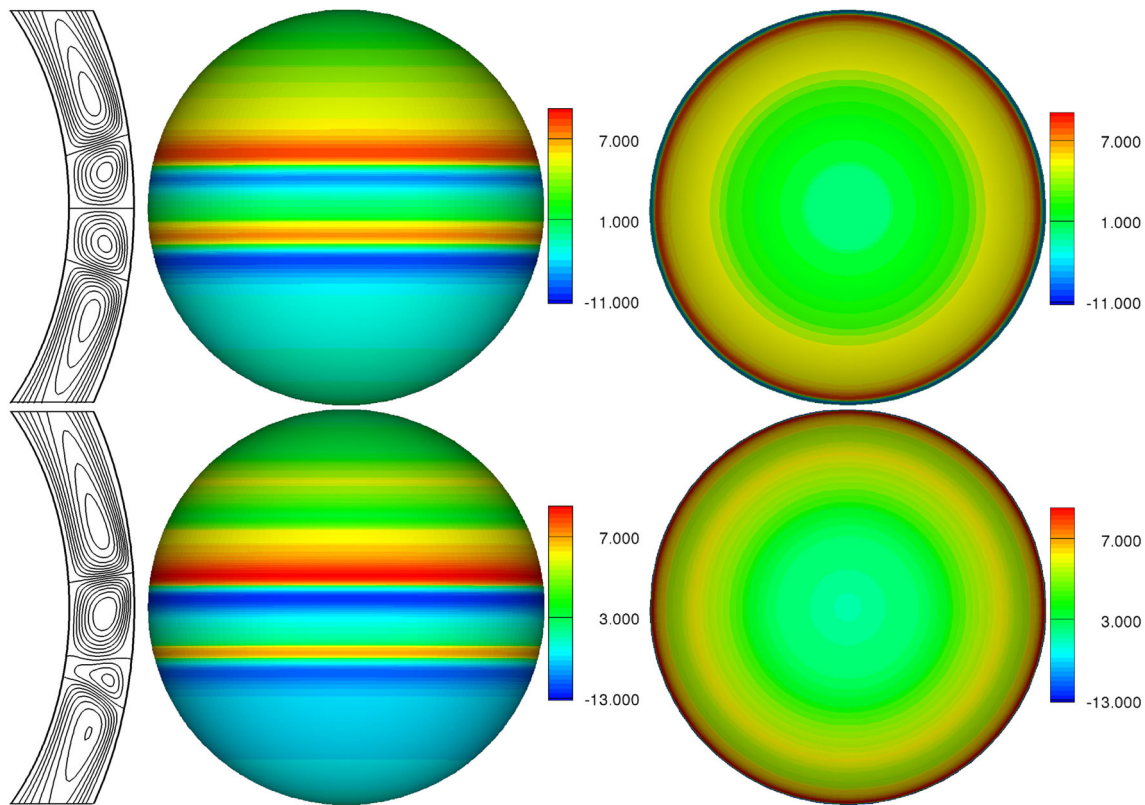


**Fig. 6** Streamlines of the symmetric 1-vortex flow at  $Re = 1400$  and the asymmetric 1-vortex flow at  $Re = 1900$  in the meridional plane ( $\phi = \pi$ ) in the equatorial region  $\frac{3\pi}{8} \leq \theta \leq \frac{5\pi}{8}$  for  $\beta = 0.33$  on the left

column, the middle column is the side view of flooded contours of the azimuthal vorticity component ( $\omega_\phi$ ) at  $r = 1 + 0.5\beta$  and the right column shows its north pole view

$\alpha = 10$  are used. The sub-iteration (pseudo-time marching) is terminated when the sub-iteration number exceeds 21. This is found sufficient to reduce the residual of the sub-iteration by two to three orders of magnitude.

### 3 Numerical results on boundary of existence of Taylor vortices

In this work, we focused on three clearance ratios,  $\beta = 0.33, 0.38$  and  $0.42$ . For each  $\beta$ , by scanning the Reynolds number range with  $\Delta Re = 100$  in a coarse search and with  $\Delta Re = 10$  in a fine search, we have determined the range  $450 \leq Re \leq 2050$  for  $\beta = 0.33$ ,  $500 \leq Re \leq 1400$  for  $\beta = 0.38$  and  $650 \leq Re \leq 1300$  for  $\beta = 0.42$  as the existence ranges for symmetric and asymmetric Taylor vortex flows respectively. It is observed that the upper boundary of  $Re$  decreases, while the lower boundary of  $Re$  increases with increasing  $\beta$ . These trends predict that the existence regime of Taylor vortices will shrink to a point in the  $(\beta, Re)$  plane at a larger  $\beta$  ( $\approx 0.48$ ). The trend that the lower boundary of  $Re$  for the occurrence of Taylor vortex increases with increasing  $\beta$  for wide-gap cases agrees with Fig. 8 given in Schrauf [9].

Figure 3 shows comparison of our numerical result for the lower boundary of existence of Taylor vortices in the  $(\beta, Re)$  plane with the numerical results of Liu et al. [31] and Schrauf [9]. The agreement is fairly good. The highest value of  $\beta$  for which we can obtain Taylor vortex flow is  $\beta = 0.48$  at  $Re = 1380$ , which is very close to that of Liu et al. [31]. It can be seen that our lower boundary curve lies above those of Schrauf [9] and Liu et al. [31]. The reason is that we have used a finer grid, which is consistent with the estimate of Schrauf [9] that high grid resolution shifts the curve upward. In figure 18, we also show the upper boundary of  $Re$  beyond which Taylor vortices collapse back to the basic flow for  $\beta \geq 0.33$ .

In the following context, we adopt the notations used by Loukopoulos and Karahalios [32] for describing the transition. The  $1a \rightarrow 1s$  represents the transition from 1-vortex asymmetric flow to 1-vortex symmetric flow,  $1a \rightarrow 0$  represents from 1-vortex asymmetric flow to symmetric 0-vortex basic flow,  $1s \rightarrow 1a$  represents from 1-vortex symmetric flow to 1-vortex asymmetric flow, and  $1s \rightarrow 0$  represents from 1-vortex symmetric flow to symmetric 0-vortex basic flow.

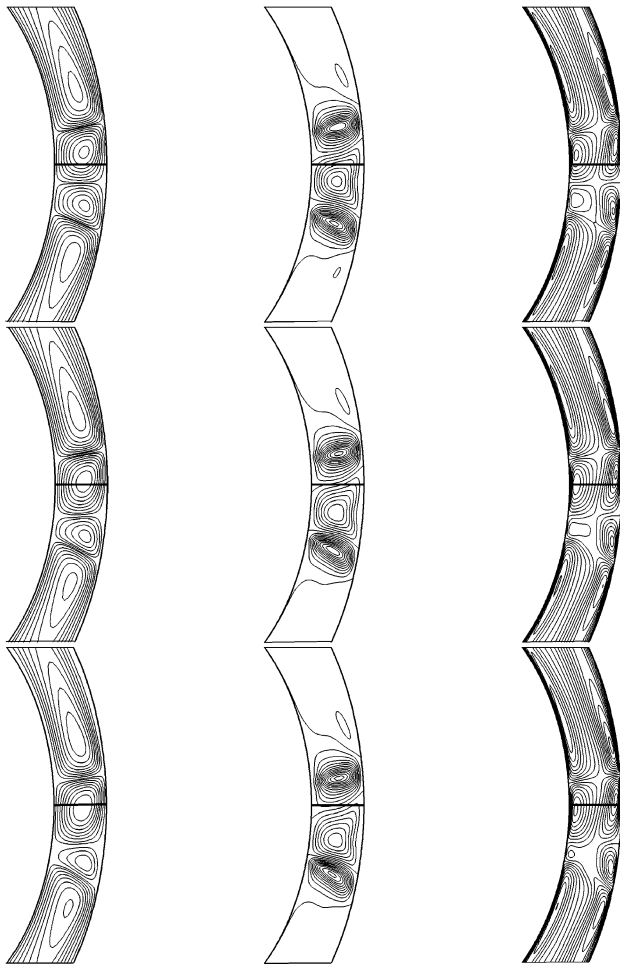


**Fig. 7** From top to bottom show the change of streamlines (left column),  $u_r$  (middle column) and  $u_\theta$  (right column) in the meridional plane ( $\phi = \pi$ ) in the equatorial region  $\frac{3\pi}{8} \leq \theta \leq \frac{5\pi}{8}$  for three times  $t = 66\pi, 100\pi$  and  $116\pi$  during the  $Re = 1900 \rightarrow 2000$  transition,  $\beta = 0.33$

## 4 Numerical results on flow structures during flow transitions

### 4.1 $\beta = 0.33$

For this clearance ratio, we have found that Taylor vortices can exist in the range  $450 \leq Re \leq 2050$ . We computed the flow using the 1-vortex flow easily produced for  $\beta = 0.18$  at  $Re = 700$  as the initial conditions and suddenly increasing  $\beta$  from 0.18 to 0.33. The approach is similar to that of Hollerbach [30], who computed symmetric and asymmetric 1-vortex flows in the range  $415 \leq Re \leq 2040$  for  $\beta = 0.336$  by starting with the stable Taylor vortex flow for  $\beta = 0.154$  and then gradually increasing  $\beta$  up to a desired value. Once we have obtained the stable 1-vortex flow for  $\beta = 0.33$  at  $Re = 700$ , we change to another Reynolds number with increment  $\Delta Re$  and march the

solution for a long time until a new stable state is reached. Using increments  $\Delta Re = 100$  and 10 we have found that the symmetric 1-vortex flow exists in  $450 \leq Re < 1850$ , and the asymmetric 1-vortex flow exists in  $1850 \leq Re \leq 2050$ . On the other hand, direct computation using the Stokes flow [7, 8] as the initial conditions can easily obtain the basic flow in the same range  $450 \leq Re \leq 2050$ . Thus, multiple solutions exist. Figure 4 shows the basic flow and the steady 1-vortex flow at  $Re_{c1} = 450$ . Both flows are symmetric with respect to the equator. The side view on the middle column shows that the vortices are toroidal, and the north pole view on the right column shows that the flow is fully axisymmetric.

As we increase the Reynolds number, the 1-vortex flow becomes more strong. To verify this, we have plotted  $u_r$  and  $u_\phi$  velocity distributions across the spherical gap on the equator at  $Re_{c1} = 450$  and  $Re = 1400$ , respectively, in Fig. 5. From the left panel it can be seen that with increasing Reynolds number, the  $u_r$  velocity increases negatively. From the right panel one can see that the portion with larger value of  $u_\phi$  shifts left because the slowly rotating fluid near the outer sphere is convected more close to the inner sphere by the jet at the equator formed between the two stronger vortices.

When we further increase the Reynolds number to  $Re_{c2} \approx 1850$ , the symmetric 1-vortex flow becomes asymmetric ( $1s \rightarrow 1a$ ) with respect to the equator, but this transition does not break the axial symmetry of the flow, and the asymmetric flow can become steady state. Figure 6 shows the symmetric vortex flow at  $Re = 1400$  and the asymmetric 1-vortex flow at  $Re = 1900$ , respectively. The meridional streamlines on the left column is in qualitative agreement with Fig. 1 in Hollerbach [30].

When we further increase the Reynolds number, the asymmetric 1-vortex flow will become time-dependent at a critical point  $Re_{c3} \approx 2000$ , and if we observe the motion in a fixed meridional plane ( $\phi = \pi$ ) the Taylor vortices look to be fluctuating. Figure 7 shows meridional streamlines,  $u_r$  and  $u_\theta$  velocity contours at three time instants,  $t = 66\pi, 100\pi$ , and  $116\pi$  for the  $Re = 1900 \rightarrow 2000$  transition. The oscillation confirms the fluctuating nature of Taylor vortices as mentioned by the axisymmetric numerical simulation of Hollerbach [30].

The fluctuations get stronger with increasing Reynolds number, but when  $Re > Re_{c4} = 2050$  the flow will collapse back to the basic state having no Taylor vortex. Figure 8 shows the four snapshots in the transition from 1-vortex asymmetric flow to 0-vortex basic flow ( $1a \rightarrow 0$ ) at  $t = 223\pi, 240\pi, 242\pi$  and  $260\pi$ , respectively, for a sudden increase of  $Re$  from 2000 to 2100. It can be seen that the streamlines on the left column are similar to the streamlines in Fig. 5 of Hollerbach [30]. Furthermore, the present

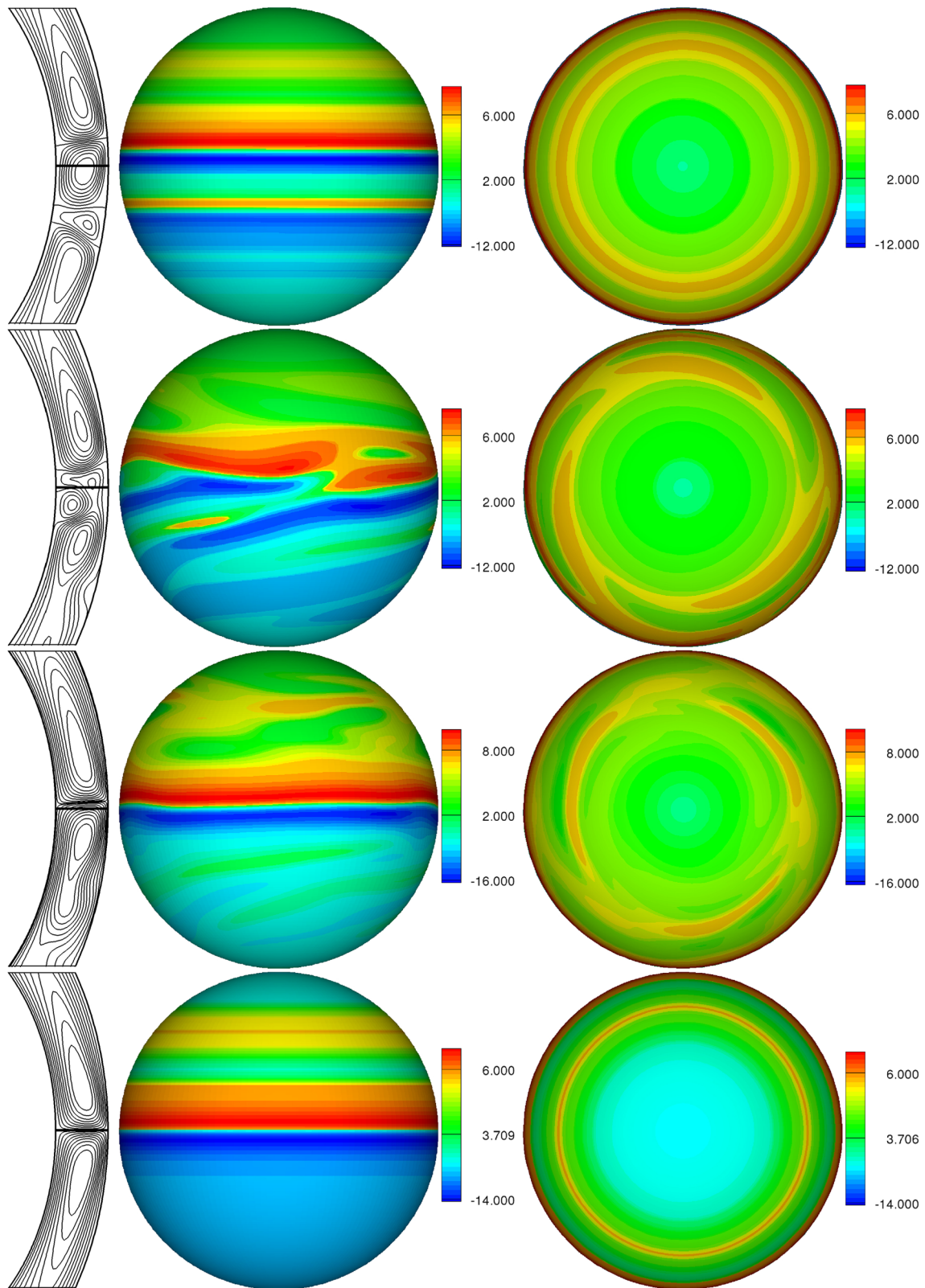


**Fig. 8** From top to bottom show snapshots at  $t = 223\pi, 240\pi, 242\pi$  and  $260\pi$  for the transition from asymmetric 1-vortex flow at  $Re = 2000$  to 0-vortex flow at  $Re = 2100$  for  $\beta = 0.33$ . The left column is the streamlines in the meridional plane ( $\phi = \pi$ ) in the equatorial

region  $\frac{3\pi}{8} \leq \theta \leq \frac{5\pi}{8}$ , the middle column is the side view of flooded contours of the azimuthal vorticity component ( $\omega_\phi$ ) at  $r = 1 + 0.5\beta$  and the right column shows its north pole view

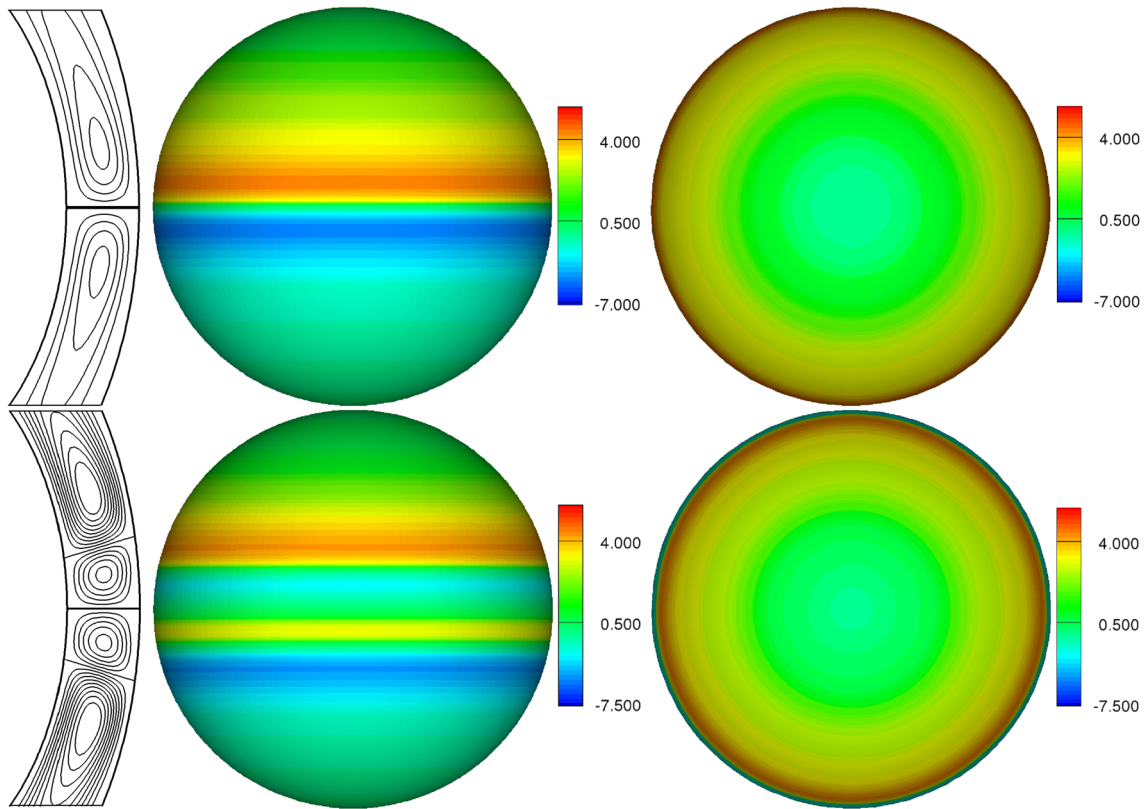


**Fig. 9** Streamlines of symmetric 0-vortex and 1-vortex flows in the meridional plane ( $\phi = \pi$ ) in the equatorial region  $\frac{3\pi}{8} \leq \theta \leq \frac{5\pi}{8}$  at  $Re_{c1} = 500$  for  $\beta = 0.38$  on the left column, middle column is the

side view of color contours of the azimuthal vorticity component ( $\omega_\phi$ ) at  $r = 1 + 0.5\beta$ , and the right column is the north pole view of it

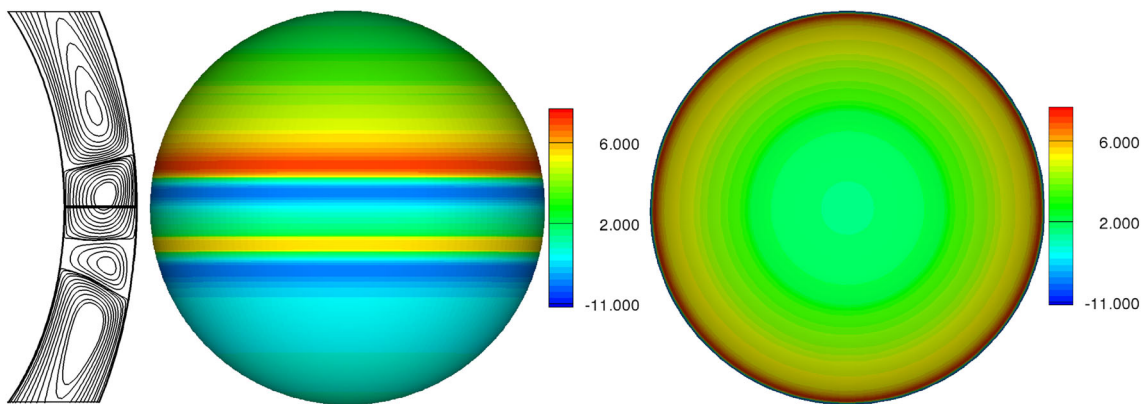


**Fig. 10** Streamlines of asymmetric 1-vortex flow in the meridional plane ( $\phi = \pi$ ) in the equatorial region  $\frac{3\pi}{8} \leq \theta \leq \frac{5\pi}{8}$  at  $Re = 1360$  for  $\beta = 0.38$  on the left, the middle is the side view of flooded contours of

the azimuthal vorticity component ( $\omega_\phi$ ) at  $r = 1 + 0.5\beta$  and the right one shows its north polar view

3D views of the azimuthal vorticity component  $\omega_\phi$  on the middle and right columns show that non-axisymmetric flow structures occur in the equatorial and middle latitude regions. At  $t = 223\pi$  in Fig. 8 the Taylor vortex flow is asymmetric about the equator and symmetric about the rotation axis. At  $t = 240\pi$  we can see that the meridional streamlines do not have complete “vortices” on the left

column, the contours of the vorticity component  $\omega_\phi$  on the middle column are distorted, and the north pole view of it on the right column shows three spiral waves. At  $t = 242\pi$ , the streamlines on the left column has almost relaxed back to the basic state, and the side view on the middle column shows regular equatorial flow again, but the north polar view on the right column shows the three spiral waves in

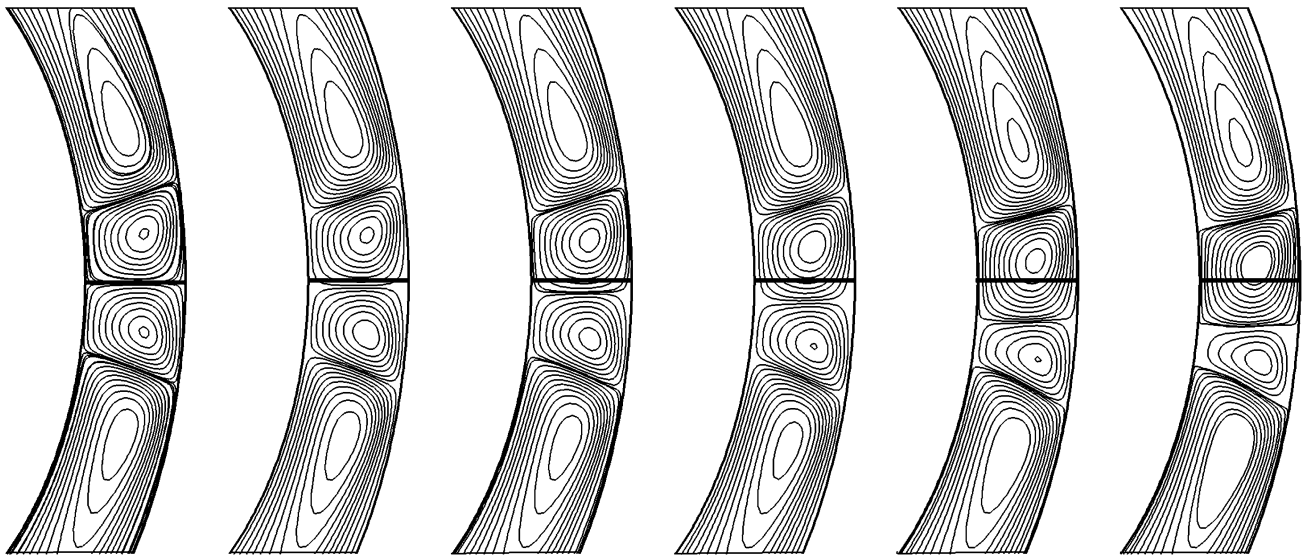


**Fig. 11** Frames from left to right show the transition from symmetric 1-vortex flow to asymmetric 1-vortex flow as  $Re = 1200 \rightarrow 1360$  in times  $t = 20\pi, 63\pi, 108\pi, 145\pi, 197\pi$  and  $230\pi$  on the meridional plane ( $\phi = \pi$ ) in the equatorial region  $\frac{3\pi}{8} \leq \theta \leq \frac{5\pi}{8}$

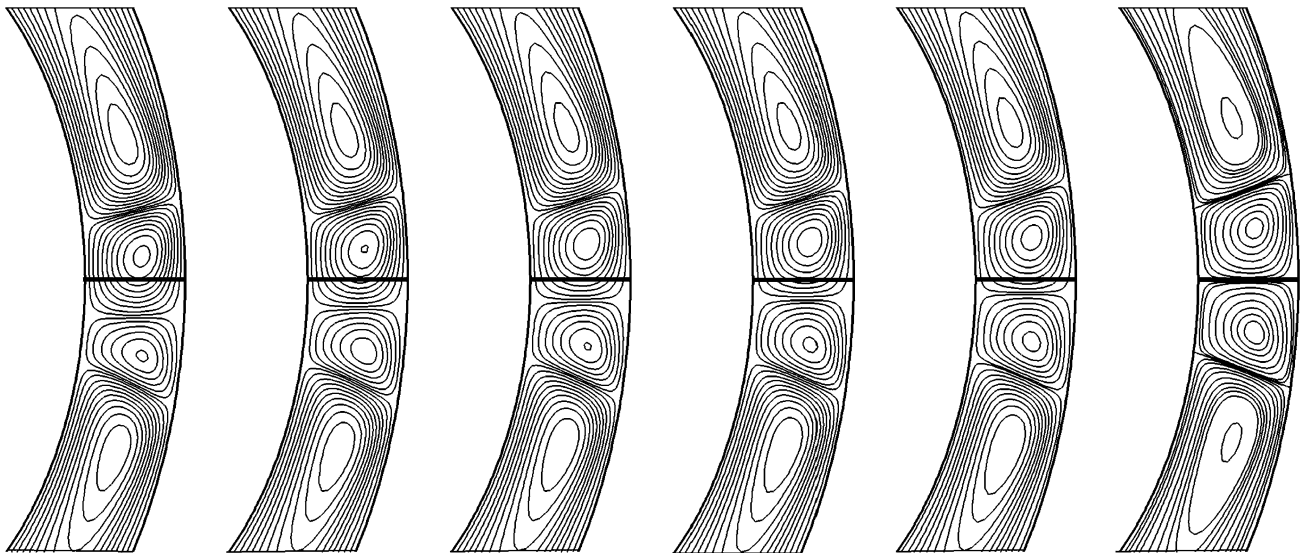


**Fig. 12** From left to right the transition of asymmetric 1-vortex flow to symmetric 1-vortex flow as  $Re = 1360 \rightarrow 1100$  in times  $t = 8\pi, 51\pi, 160\pi, 258\pi, 410\pi$  and  $600\pi$  on the meridional plane ( $\phi = \pi$ ) in the equatorial region  $\frac{3\pi}{8} \leq \theta \leq \frac{5\pi}{8}$

the polar region are still changing. Finally at  $t = 260\pi$ , the flow collapses back to the basic state having no Taylor vortices and becomes completely axisymmetric. The  $1a \rightarrow 0$  transition is due to the instabilities occurring in a smaller vortex between two oppositely directed large vortices when it is looked at from a fluid dynamics point of view, or is due to the expansion of chaotic solutions when it is looked at from a dynamical system point of view [30].

#### 4.2 $\beta = 0.38$

For this clearance ratio, Taylor vortices exist in the range  $500 \leq Re \leq 1400$ . To get Taylor vortices we have used the 1-vortex flow obtained for  $\beta = 0.18$  at  $Re = 700$  as the initial conditions the same as for  $\beta = 0.33$ . By varying the Reynolds number, we found that steady 1-vortex flow starts to appear at  $Re_{c1} \approx 500$ , and can exist up to  $Re_{c3} \approx 1400$ . Figure 9 shows symmetric 0-vortex and 1-vortex flows coexisting at  $Re_{c1} = 500$ . The steady 0-vortex flow is obtained using the Stokes flow as the initial conditions.

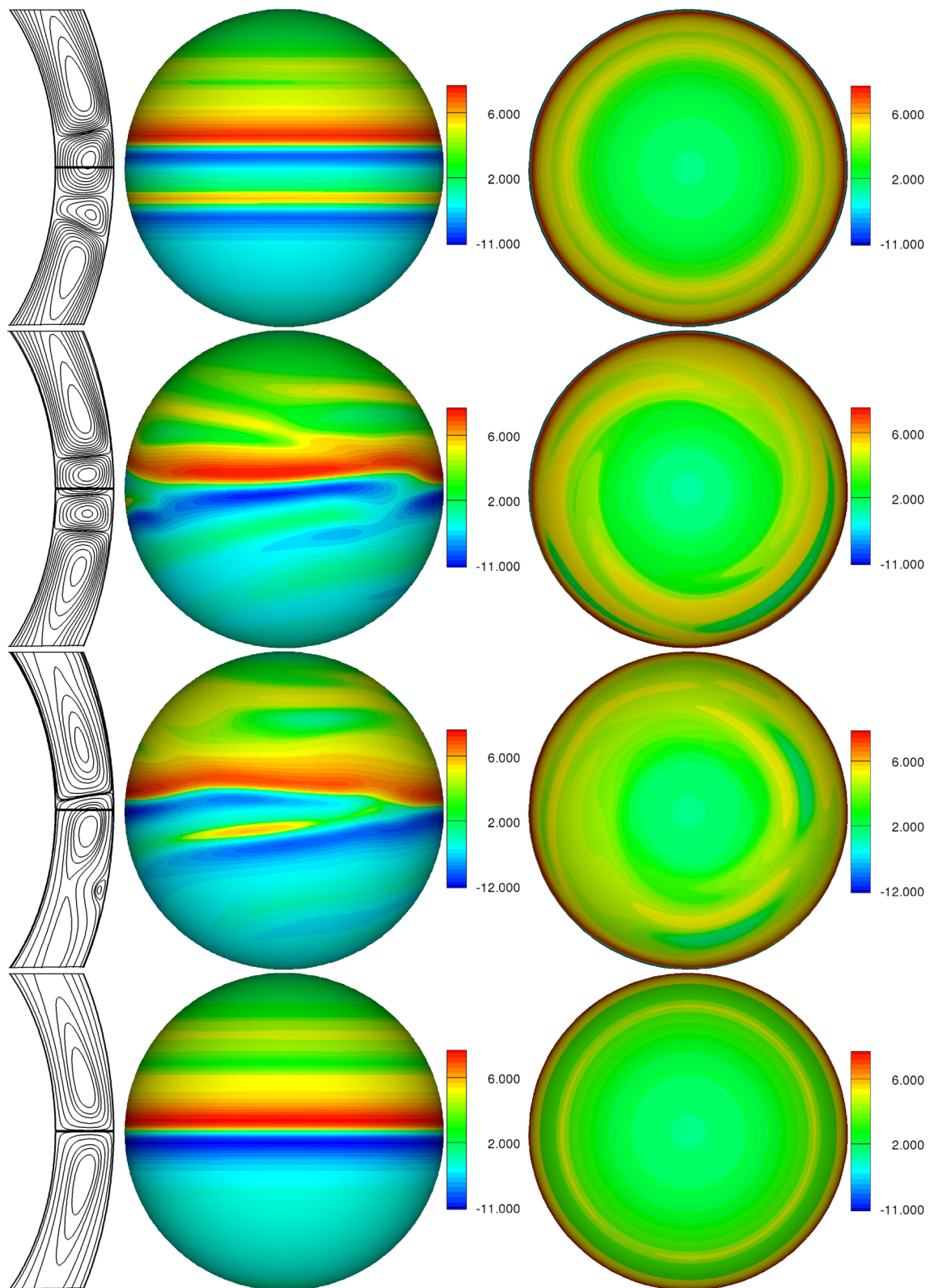


**Fig. 13** From top to bottom transition from asymmetric 1-vortex flow at  $Re = 1360$  to 0-vortex basic state at  $Re = 1450$  at  $t = 36\pi, 51\pi, 57\pi$  and  $72\pi$  on the meridional plane ( $\phi = \pi$ ) in the equatorial region  $\frac{3\pi}{8} \leq \theta \leq \frac{5\pi}{8}$  for  $\beta = 0.38$  in the left column, the

middle column is the side view of color contours of the azimuthal vorticity component ( $\omega_\phi$ ) at  $r = 1 + 0.5\beta$  and the right column shows its north pole view

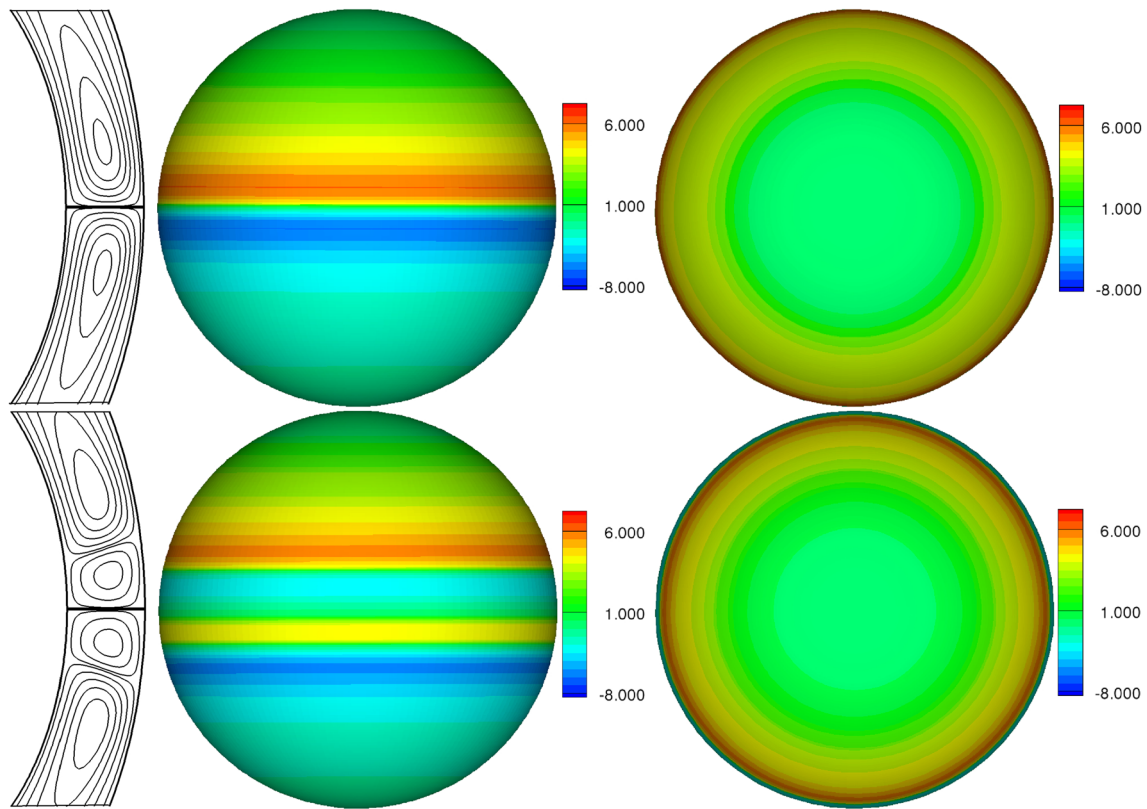


**Fig. 14** Streamlines of symmetric 0-vortex and 1-vortex flows in the meridional plane ( $\phi = \pi$ ) in the equatorial region  $\frac{3\pi}{8} \leq \theta \leq \frac{5\pi}{8}$  at  $Re_{c1} = 650$  for  $\beta = 0.42$  on the left column, the middle column is the

side view of color contours of the azimuthal vorticity component ( $\omega_\phi$ ) at  $r = 1 + 0.5\beta$ , and the right column is the north pole view of it

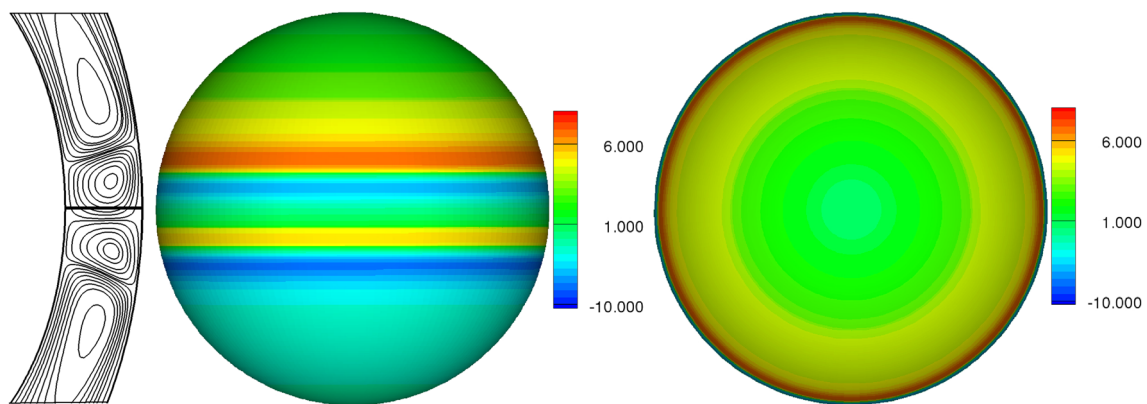


**Fig. 15** Streamlines of asymmetric 1-vortex flow in the meridional plane ( $\phi = \pi$ ) in the equatorial region  $\frac{3\pi}{8} \leq \theta \leq \frac{5\pi}{8}$  at  $Re_{c2} = 1150$  for  $\beta = 0.42$  on the left, the middle is the side view of flooded contours of

the azimuthal vorticity component ( $\omega_\phi$ ) at  $r = 1 + 0.5\beta$  and the right one shows its north polar view

By increasing the Reynolds number a bit larger than  $Re_{c2} \approx 1210$  the steady symmetric 1-vortex flow becomes steady asymmetric 1-vortex flow. This bifurcation is characterized as pitchfork bifurcation by Vassilios and George [32] because at this point the symmetric flow exchanges stability with a pair of asymmetric flows. In fluid mechanical systems, this sudden symmetric branching

is given the name of pitchfork symmetry breaking bifurcation. Figure 10 shows a typical steady asymmetric 1-vortex flow at  $Re = 1360$ , and it is observed that this asymmetric flow state has a good resemblance to figure 1c of Loukopoulos and Karahalios [32].

Figure 11 shows the time evolution from the symmetric Taylor vortex flow at  $Re = 1200$  to asymmetric one ( $1s \rightarrow$

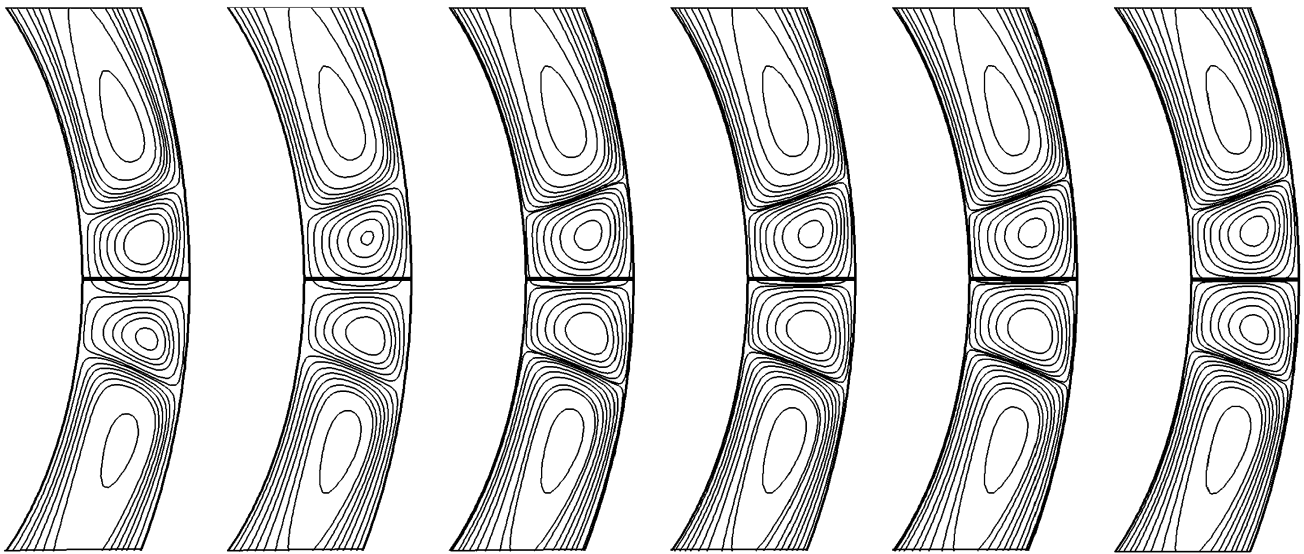


**Fig. 16** From left to right the transition from asymmetric 1-vortex flow to symmetric 1-vortex flow as the Reynolds number  $Re = 1150 \rightarrow 1050$  in time instants,  $t = 10\pi, 26\pi, 85\pi, 128\pi, 192\pi$  and  $300\pi$  on the meridional plane ( $\phi = \pi$ ) in the equatorial region  $\frac{3\pi}{8} \leq \theta \leq \frac{5\pi}{8}$

1a) at  $Re = 1360$ . The Reynolds number is increased to 1360 abruptly, the flow becomes asymmetric with respect to the equator. We can see that the Taylor vortices keep the shape in the transition. This is because there is no breaking of axisymmetry in the transition.

To connect the regions of supercritical flows with possible transition, we start from the steady asymmetric flow state at  $Re = 1360$  and abruptly reduce the Reynolds number to 1100. We find that the asymmetric Taylor vortex flow becomes steady-state symmetric Taylor vortex flow after a very long time period of  $600\pi$ . Figure 12 shows the transition from asymmetric state to symmetric state ( $1a \rightarrow 1s$ ).

Next, to simulate the  $1a \rightarrow 0$  transition with increasing Reynolds number, we start with the asymmetric flow state at  $Re = 1360$  and increase the Reynolds number to  $Re = 1450 > Re_{c3} \approx 1400$  suddenly. Four instants spanning  $72\pi$  of time in the  $1a \rightarrow 0$  transition are shown in Fig. 13. The left column shows meridional streamlines in a meridional plane, the middle and right columns show 3D views of the azimuthal vorticity components  $\omega_\phi$ . At  $t = 0$ , the Reynolds number is suddenly increased to  $Re = 1450$  from  $Re = 1360$ . At the first instant  $t = 36\pi$  the flow has some 3D disturbances in the middle latitude region. The north pole view of the vorticity in the right column shows a symptom of three spiral waves. At the second instant  $t = 51\pi$  we can see that the three spiral waves are going toward the equatorial region on the middle and right columns. At the third instant  $t = 57\pi$  the streamlines in the left column is rather temporal because there are transient structures as shown on the middle and right columns, where the spiral-like waves in the high latitude region become weaker. As

time goes on, the waves in the middle latitude region becomes more irregular and weaker and then the flow collapses back to basic state having no Taylor vortices, and then gradually recover equatorial and axial symmetry at the fourth instant  $t = 72\pi$ .

### 4.3 $\beta = 0.42$

For this clearance ratio, the Taylor vortex flow exists in  $650 \leq Re \leq 1300$ . The technique to get the Taylor vortices is the same as for  $\beta = 0.33$ . Figure 14 shows the 0-vortex basic flow and symmetric 1-vortex flow coexisting at  $Re_{c1} \approx 650$ .

By increasing the Reynolds number the symmetric 1-vortex flow at  $Re_{c1} = 650$  becomes steady asymmetric 1-vortex flow at  $Re_{c2} = 1150$  as shown in Fig. 15.

To connect the regions of supercritical flows with possible transitions we start from the asymmetric flow at  $Re_{c2} = 1150$  in Fig. 15 and then abruptly reduce the Reynolds number to 1050. We found that the asymmetric flows becomes steady symmetric flow after a long time of  $300\pi$ . Figure 16 shows the transition from asymmetric state to symmetric state ( $1a \rightarrow 1s$ ). Our calculations verified that the critical Reynolds number is the same for ( $1s \rightarrow 1a$ ) and ( $1a \rightarrow 1s$ ) transitions. So the  $1s \rightarrow 1a$  transition is related to a pitchfork bifurcation.

To simulate the  $1a \rightarrow 0$  transition with increasing  $Re$ , we start from the asymmetric 1-vortex flow at  $Re_{c2} = 1150$  in Fig. 15, and suddenly increase the Reynolds number to  $1350 > Re_{c3} \approx 1300$ . The  $1a \rightarrow 0$  transition is finished after a time period of  $134\pi$  as shown in Fig. 17. The 3D patterns in terms of the azimuthal vorticity components  $\omega_\phi$

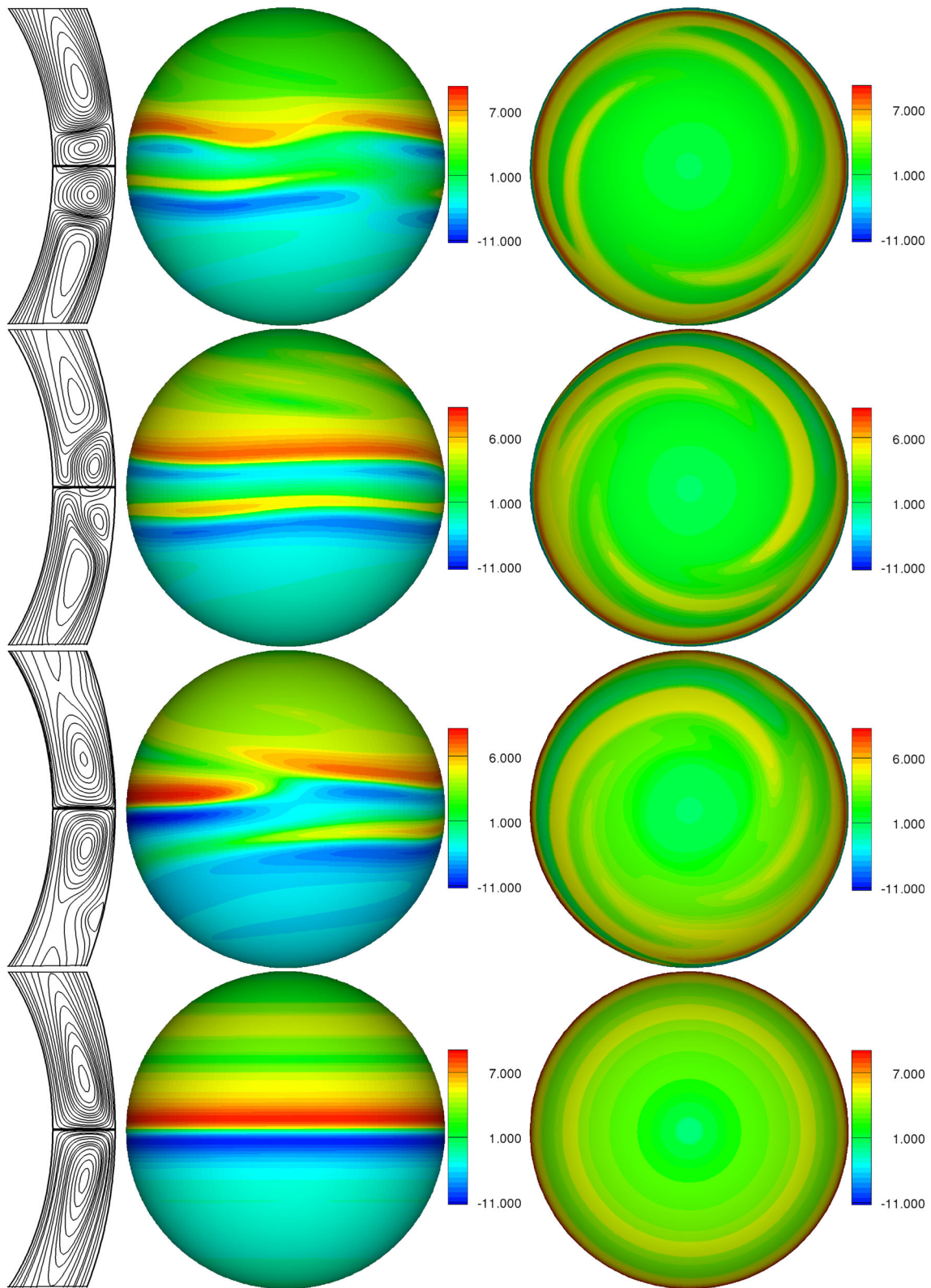


**Fig. 17** From top to bottom transition from asymmetric 1-vortex flow at  $Re_{c2} = 1150$  to 0-vortex basic flow at  $Re = 1350$  at  $t = 94\pi, 97\pi, 100\pi$  and  $134\pi$  on the meridional plane ( $\phi = \pi$ ) in the equatorial region  $\frac{3\pi}{8} \leq \theta \leq \frac{5\pi}{8}$  for  $\beta = 0.42$  in the left column, the

middle column is the side view of flooded contours of the azimuthal vorticity component ( $\omega_\phi$ ) at  $r = 1 + 0.5\beta$  and the right column shows its north pole view

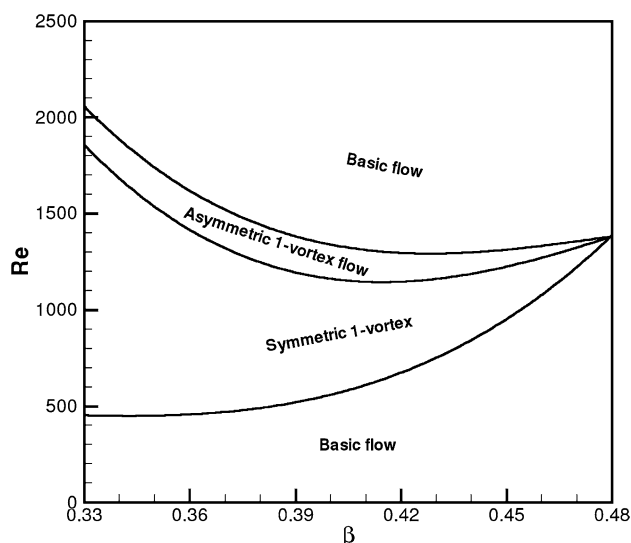


**Fig. 18** Existence regimes of different flow states for wide gap cases. Notice that the basic flow also exists in the regimes of symmetric and asymmetric Taylor vortex flows

on the middle and right columns are similar to those for  $\beta = 0.33$  and  $\beta = 0.38$ , so we will not describe them in detail here.

Finally, Fig. 18 gives the existence regimes in the  $(\beta, Re)$  plane for the basic flow and the symmetric and asymmetric Taylor vortex flows. This graph may be a supplement to the well-known regime graph of various disturbances in the  $(\beta, Re)$  plane as given by Nakabayashi et al. [34].

## 5 Conclusions

We have investigated the existence regime of symmetric and asymmetric Taylor vortices in wide-gap spherical Couette flow with only the inner sphere rotating. Using the 1-vortex flow for a medium gap  $\beta = 0.18$  as the initial conditions, we have obtained the existence regime of Taylor vortices for  $\beta > 0.33$  in the  $(\beta, Re)$  plane.

Three wide-gap clearance ratios  $\beta = 0.33, 0.38$  and  $0.42$  have been studied in detail. For  $\beta = 0.33$ , Taylor vortices can exist in the range of  $450 \leq Re \leq 2050$ . Symmetric steady 1-vortex flow can exist at  $Re_{c1} = 450$ . With increasing  $Re$ , the symmetric flow becomes steady asymmetric Taylor vortex flow at  $Re_{c2} = 1850$  through a transition without breaking the axial symmetry. Increasing  $Re$  further, the asymmetric flow becomes unsteady at  $Re_{c3} = 2050$ . This confirms the time-dependent behavior in the meridional flow in [30]. With increasing Reynolds number further the flow returns back to the 0-vortex basic flow state via a fully three-dimensional transition. The critical Reynolds numbers ( $Re_{c1} = 450, Re_{c3} = 2050$ ) and

the meridional streamline patterns are in good agreement with available numerical and experimental results of (470, 1850), (415, 2040), (467, 2100) in [29–31] respectively.

For  $\beta = 0.38$ , Taylor vortices can exist in  $500 \leq Re \leq 1400$ . The steady symmetric 1-vortex flow becomes steady asymmetric at  $Re_{c2} = 1200$ . Further increasing the Reynolds number above  $Re_{c3} = 1400$  the asymmetric 1-vortex flow undergoes a fully 3D transition and then collapses back to the steady basic state. No time-dependent flow regime is found. The meridional streamlines are similar to the numerical results of Loukopoulos and Karahalios [32].

For  $\beta = 0.42$ , Taylor vortices exist in the range  $650 \leq Re \leq 1300$ . With increasing Reynolds number, the steady symmetric 1-vortex flow becomes steady asymmetric at  $Re_{c2} = 1150$ . Further increasing the Reynolds number above  $Re_{c3} = 1300$  the asymmetric flow undergoes a fully 3D stage and returns back to the steady basic flow. The critical Reynolds numbers and the meridional streamlines are found in good agreement with the numerical results [32].

**Acknowledgements** This work is supported by Natural Science Foundation of China (11321061, 11261160486, and 91641107), and Fundamental Research of Civil Aircraft (MJ-F-2012-04). Suhail Abbas thanks the support of CAS-TWAS President's Fellowship Program to finance his PhD in University of Chinese Academy of Sciences, Beijing, China.

## References

1. Roesner KG (1978) Numerical calculation of hydrodynamic stability problems with time-dependent boundary conditions. In: Proceedings of the international conference on numerical methods in fluid dynamics, pp 1–25
2. Wimmer M (1988) Viscous flow and instabilities near rotating bodies. *Prog Aerosp Sci* 25:43–103
3. Sha W, Nakabayashi K (2001) On the structure and formation of spiral Taylor–Görtler vortices in spherical Couette flow. *J Fluid Mech* 431:323–345
4. Yuan L (2012) Numerical investigation of wavy and spiral Taylor–Görtler vortices in medium spherical gaps. *Phys Fluids* 24:124104
5. Yuan L (2004) Numerical study of multiple periodic flow states in spherical Taylor–Couette flow. *Sci China Ser A* 4:81–91
6. Yuan L, Fu DX, Ma YW (1996) Numerical study of bifurcation solutions of spherical Taylor–Couette flow. *Sci China Ser A* 39(2):187–196
7. Marcus P, Tuckerman L (1987) Simulation of flow between two concentric rotating spheres Part 1: steady states. *Fluid Mech* 185:1–30
8. Marcus P, Tuckerman L (1987) Simulations of flow between two concentric rotating spheres. Part 2: transitions. *Fluid Mech* 185:31–65
9. Schrauf G (1986) The first instability in spherical Couette flow. *J Fluid Mech* 166:287–303

10. Buhler K, Zierep J (1987) Dynamical instabilities and transition to turbulence in spherical gap flows. In: Comte-Bellot G, Mathieu J (eds) Proceedings of the 1st European turbulence conference on advances in turbulence, vol 16. Springer, Berlin
11. Bartels F (1982) Taylor vortices between two-concentric rotating spheres. *J Fluid Mech* 119:1–65
12. Yavorskaya I, Belyaev Y, Monakhov A, Astaf N, Scherbakov S, Vvedenskaya N (1980) Stability, nonuniqueness and transition to turbulence in the flow between two rotating spheres. Report No. 595, Space Research Institute of the Academy of Science. USSR
13. Wimmer M (1976) Experiments on a viscous fluid flow between concentric rotating spheres. *J Fluid Mech* 78:317–335
14. Munson B, Menguturk M (1975) Viscous incompressible flow between concentric rotating spheres. Part 3. Linear stability. *J Fluid Mech* 69:281–318
15. Sawatzki O, Zierep J (1970) Das Stromfeld im Spalt zwischen zwei konzentrischen Kulgelflachen, von denen die innere rotiert. *Acta Mech* 9:13–35
16. Nakabayashi K (1983) Transition of Taylor–Gortler vortex flow in spherical Couette flow. *J Fluid Mech* 132:209–230
17. Nakabayashi K, Tsuchida Y (1995) Flow-history effect on higher modes in the spherical Couette flow. *J Fluid Mech* 295:43–60
18. Zikanov O (1996) Symmetry-breaking bifurcations in spherical Couette flow. *J Fluid Mech* 310:293–324
19. Mahloul M, Mahamdia A, Kristiawan A (2016) The spherical Taylor–Couette flow. *Eur J Mech B/Fluids* 59:1–6
20. Mahloul M, Mahamdia A, Kristiawan A (2016) Experimental investigations of the spherical Taylor–Couette flow. *J Appl Fluid Mech* 9:131–137
21. Lalaoua A, Bouabdallah A (2016) A numerical investigation on the onset of the various flow regimes in a spherical annulus. *J Fluids Eng* 138:1–11
22. Child A, Hollerbach R, Kersale E (2017) Axisymmetric pulse train solutions in narrow-gap spherical Couette flow. *Phys D* 348:54–59
23. Wulf P, Egbers C, Rath HJ (1999) Routes to chaos in wide-gap spherical Couette flow. *Phys Fluids* 11:1359–1372
24. Egbers C, Rath HJ (1995) The existence of Taylor vortices and wide-gap instabilities in spherical Couette flow. *Acta Mech* 111:125–140
25. Hollerbach R, Junk M, Egbers C (2006) Non-axisymmetric instabilities in basic state spherical Couette flow. *Fluid Dyn Res* 38:257–273
26. Dumas G (1991) Study of spherical Couette flow via 3D spectral simulations: large and narrow gap flows and their transitions. Ph.D. Thesis, California Institute of Technology
27. Dumas G, Leonard A (1994) A divergence-free spectral expansions method for three-dimensional flows in spherical-gap geometries. *J Comput Phys* 111:205–219
28. Araki K, Mizushima J, Yanase S (1997) The nonaxisymmetric instability of the wide-gap spherical Couette flow. *Phys Fluids* 9:1197–1199
29. Junk M, Egbers C (2000) Isothermal spherical Couette flow. In: Egbers C, Pfister G (eds) Physics of rotating fluids. Lecture notes in physics, vol 549. Springer, Berlin, pp 215–235
30. Hollerbach R (1998) Time-dependent Taylor vortices in wide-gap spherical Couette flow. *Phys Rev Lett* 81:31–32
31. Liu M, Blohm C, Egber C, Wulf P, Rath HJ (1996) Taylor vortices in wide spherical shell. *Phys Rev Lett* 77:286
32. Loukopoulos C, Karahalios T (2004) Taylor vortices in annular spherical flow at large aspect ratios. *Phys Fluids* 16:2708–2711
33. Abbas S, Yuan L, Shah, A (2017) Simulation of spiral instabilities in wide-gap spherical Couette flow. *Fluid Dyn Res*. <https://doi.org/10.1088/1873-7005/aa9d77>
34. Nakabayashi K, Tsuchida Y, Zheng Z (2002) Characteristics of disturbances in the laminar-turbulent transition of spherical Couette flow. 1. Spiral Taylor–Gortler vortices and traveling waves for narrow gaps. *Phys Fluids* 14(11):3963–3972
35. Zhilenko DY, Krivososova OE, Nikitin NV (2007) Direct numerical simulation of the laminar-turbulent transition in a thick spherical layer. *Fluid Dyn* 42(6):886–896
36. Yang JY, Yang SC, Chen YN, Hsu CA (1998) Implicit weighted ENO schemes for three-dimensional incompressible Navier–Stokes equations. *J Comput Phys* 146:464–487
37. Rogers S, Kwak D (1990) Upwind differencing scheme for the time-accurate incompressible Navier–Stokes equations. *AIAA J* 28:253
38. Rogers S, Kwak D, Kiris C (1991) Steady and unsteady solutions of the incompressible Navier–Stokes equations. *AIAA J* 29:603–610
39. Shah A, Yuan L, Islam S (2012) Numerical solution of unsteady Navier–Stokes equations on curvilinear meshes. *Comput Maths Appl* 63:1548–1556
40. Yuan L (2002) Comparison of implicit multigrid schemes for three-dimensional incompressible flows. *J Comput Phys* 77:134–155
41. Chorin A (1967) A numerical method for solving incompressible viscous flow problems. *J Comput Phys* 2:12–26
42. Jiang GS, Wu CC (1999) A high-order WENO finite difference scheme for the equations of ideal magnetohydrodynamics. *J Comput Phys* 150:561–594